IJMMM International Journal of Minerals, Metallurgy and Materials 矿物冶金与材料学报（英文版）

Oxidation behavior of FeV_2O_4 and $FeCr_2O_4$ particles in the air: Nonisothermal kinetic and reaction mechanism

Junyi Xiang, Xi Lu, Luwei Bai, Hongru Rao, Sheng Liu, Qingyun Huang, Shengqin Zhang, Guishang Pei, and Xuewei Lü

Cite this article as:
Junyi Xiang, Xi Lu, Luwei Bai, Hongru Rao, Sheng Liu, Qingyun Huang, Shengqin Zhang, Guishang Pei, and Xuewei Lü, Oxidation behavior of FeV_2O_4 and $FeCr_2O_4$ particles in the air: Nonisothermal kinetic and reaction mechanism, *Int. J. Miner. Metall. Mater.*, 31(2024), No. 8, pp. 1839-1848. https://doi.org/10.1007/s12613-024-2851-6

View the article online at SpringerLink or IJMMM Webpage.

INTERNATIONAL JOURNAL OF
Minerals, Metallurgy and Materials

Volume 31, Number 8, August 2024
Page 1839

Research Article https://doi.org/10.1007/s12613-024-2851-6

Oxidation behavior of FeV_2O_4 and $FeCr_2O_4$ particles in the air: Nonisothermal kinetic and reaction mechanism

Junyi Xiang[1),✉], *Xi Lu*[1)], *Luwei Bai*[1)], *Hongru Rao*[1)], *Sheng Liu*[1)], *Qingyun Huang*[1)], *Shengqin Zhang*[1)], *Guishang Pei*[2),✉], *and Xuewei Lü*[3)]

1) School of Metallurgy and Materials Engineering, Chongqing University of Science and Technology, Chongqing 401331, China
2) Department of Materials Science and Engineering, Seoul National University, Seoul 08826, Rep. of Korea
3) College of Materials Science and Engineering, Chongqing University, Chongqing 400044, China
(Received: 27 November 2023; revised: 5 February 2024; accepted: 6 February 2024)

Abstract: High-temperature oxidation behavior of ferrovanadium (FeV_2O_4) and ferrochrome ($FeCr_2O_4$) spinels is crucial for the application of spinel as an energy material, as well as for the clean usage of high-chromium vanadium slag. Herein, the nonisothermal oxidation behavior of FeV_2O_4 and $FeCr_2O_4$ prepared by high-temperature solid-state reaction was examined by thermogravimetry and X-ray diffraction (XRD) at heating rates of 5, 10, and 15 K/min. The apparent activation energy was determined by the Kissinger–Akahira–Sunose (KAS) method, whereas the mechanism function was elucidated by the Malek method. Moreover, *in-situ* XRD was conducted to deduce the phase transformation of the oxidation mechanism for FeV_2O_4 and $FeCr_2O_4$. The results reveal a gradual increase in the overall apparent activation energies for FeV_2O_4 and $FeCr_2O_4$ during oxidation. Four stages of the oxidation process are observed based on the oxidation conversion rate of each compound. The oxidation mechanisms of FeV_2O_4 and $FeCr_2O_4$ are complex and have distinct mechanisms. In particular, the chemical reaction controls the entire oxidation process for FeV_2O_4, whereas that for $FeCr_2O_4$ transitions from a three-dimensional diffusion model to a chemical reaction model. According to the *in-situ* XRD results, numerous intermediate products are observed during the oxidation process of both compounds, eventually resulting in the final products $FeVO_4$ and V_2O_5 for FeV_2O_4 and Fe_2O_3 and Cr_2O_3 for $FeCr_2O_4$, respectively.

Keywords: FeV_2O_4; $FeCr_2O_4$; oxidation; nonisothermal kinetics; mechanism

1. Introduction

Crystalline materials with spinel structure and general chemical formula AB_2X_4 (A and B are usually metal cations) have been widely studied for their magnetic and dielectric properties [1–3] and remarkable material applications. For example, the well-known ferrovanadium spinel (FeV_2O_4) and ferrochrome spinel ($FeCr_2O_4$) compounds with unique crystal structures exhibit normal cubic spinel structures at room temperature (space group $Fd\bar{3}m$) [4–6].

Spinel structure materials have recently attracted widespread technological attention owing to their exceptional electromagnetic properties [7–10]. Spinel FeV_2O_4 exhibits large capacity and high abundance, making it a crucial anode material for lithium-ion batteries and electronic devices [11–13], has potential as a photoelectric material and catalyst with broad application prospects [14–16], and in combination with other compounds, demonstrates boosted antibacterial properties [17–18]. Spinel $FeCr_2O_4$ has wide applications in photocatalysis [19], pollutant degradation [20], and gas sensing [8] owing to its excellent electrocatalytic activity and stability. Although both spinels show superiority in several applications, their efficacy may be compromised by oxidation at high temperatures and complex environmental conditions [21–24].

Spinel FeV_2O_4 and spinel $FeCr_2O_4$ are also the predominant phases in high-chromium vanadium slag [25]. However, owing to the similar physical and chemical properties of vanadium and chromium, extracting these oxides from high-chromium vanadium slag presents significant challenges [26–27]. The primary method for vanadium extraction is sodium roasting–water leaching vanadium extraction; however, during roasting, competition between sodium vanadate and sodium chromate formed by oxidation and combination with sodium salts, respectively, results in significant competition between them. The selective separation of vanadium and chromium by roasting–leaching challenges achieving clean usage of such slag. Thus, elucidating the oxidation evolution law of ferrovanadium and ferrochrome spinels during oxidation roasting is essential for improving the vanadium recovery rate.

This study presents the successful preparation of high

✉ Corresponding authors: Junyi Xiang E-mail: xiangjunyi126@126.com; Guishang Pei E-mail: peiguishang@snu.ac.kr

crystallinity pure FeV_2O_4 and $FeCr_2O_4$ by high-temperature solid-state reaction. Their oxidation behavior in air is extensively examined for the first time by thermogravimetry (TG) and *in-situ* X-ray diffraction (XRD). The focus of this study was to understand both compounds' oxidation reactions at high temperatures as well as phase transitions at different temperatures and determine the final products. This study provides a theoretical basis for the applications of spinel materials in batteries, catalysts, and oxidation roasting–leaching processes of vanadium chromium slag.

2. Experimental

2.1. Materials preparation

FeV_2O_4 was synthesized by high-temperature solid-state reaction. Briefly, V_2O_3 (>99.9% purity, Shanghai Mackin Biochemical Co. Ltd., China) and Fe_2O_3 (99.99% purity, Aladdin Chemical Reagent Co. Ltd., China) were stoichiometrically weighed and thoroughly mixed before being finely ground into powder using an agate motor by adding ethanol as required. Then, the mixture was loaded into a molybdenum crucible and placed in a tube furnace (GSL-1700X-VT, Hefei Kejing Group, China). The temperature was gradually increased from room temperature to 1200°C at 5 K/min and held at this temperature for 12 h. A gas mixture (volume ratio is CO_2/H_2 = 0.7) was continuously flown through the tube at 200 mL/min during the heating and cooling stages [28–29]. Finally, the product was cooled to ambient temperature within the furnace before being ground for subsequent characterization.

$FeCr_2O_4$ was prepared by the above method but with Fe_2O_3 (99.99% purity, Aladdin Chemical Reagent Co. Ltd., China) and Cr_2O_3 (>99.9% purity, Shanghai Mackin Biochemical Co. Ltd., China) as starting materials.

2.2. Thermogravimetric analysis

TG analyzer (Setaram Evo TG-DTG 1750, Setaram Instrumentation, France) was used for nonisothermal oxidation tests of FeV_2O_4 ($FeCr_2O_4$) powders. Approximately 20 mg of sample was loaded into an alumina crucible and then heated in a dynamic air atmosphere at 20 mL/min from room temperature to 700°C (900°C) at three heating rates (β) of 5, 10, and 15 K/min.

2.3. Thermodynamic analysis and characterization

Thermodynamic analysis was conducted with FactSage 8.1, in which Gibbs-free energies of the chemical reactions were calculated using the reaction module. The FactPS and FToxid databases were applied.

The crystal structures of the synthesized FeV_2O_4 and $FeCr_2O_4$, as well as their oxidation products, were characterized using an XRD (Aeries, Malvern Panalytical, Netherlands) with Cu K_α radiation at 40 kV and 8 mA. An *in-situ* XRD with Cu K_α radiation (Empyrean, PANalytical B.V., Holland) equipped with platinum heating components and a corundum crucible was used in the experiments to determine the phase composition during the solid reaction process at high temperatures for a better understanding of the reaction process. Phase analysis and Rietveld refinement were performed using High-score Plus 5.0 software with the international centre for diffraction date (ICDD) database.

3. Results and discussion

3.1. Characterization of FeV_2O_4 and $FeCr_2O_4$

Fig. 1 presents the XRD patterns and Rietveld graphs of the synthesized FeV_2O_4 and $FeCr_2O_4$. The XRD pattern and Rietveld graph of the synthesized FeV_2O_4 in Fig. 1(a) show excellent agreement with the standard JCPDS (No. 96-901-2330) pattern of coulsonite (FeV_2O_4) of cubic phase with space group $Fd\bar{3}m$, demonstrating a high level of conformity. Refinement with *R*-weighted pattern (R_{wp}) obtained an impressively low R_{wp} value (2.53%), showing a highly reliable refinement procedure. The refined unit cell parameters for the crystal structure were $a = b = c = 8.4562$ Å, closely matching those reported in JCPDS No. 96-901-2330 ($a = b = c = 8.4530$ Å). The XRD pattern and Rietveld graph of the synthesized $FeCr_2O_4$ in Fig. 1(b) show good agreement with the standard JCPDS (No. 00-034-0140) pattern of coulsonite ($FeCr_2O_4$) belonging to the cubic phase with space group $Fd\bar{3}m$, further confirming its accuracy with a low R_{wp} value (3.56%). The refined unit cell parameters for the crystal structure were $a = b = c = 8.3780$ Å, closely resembling those in JCPDS No. 00-034-0140 ($a = b = c = 8.3790$ Å).

3.2. TG-DTG analysis

Fig. 2 presents the TG curves of FeV_2O_4 and $FeCr_2O_4$ at different heating rates in air. The FeV_2O_4 exhibits a slow rate of oxidation below 400°C with a minimal weight increase of less than 1.00wt%. Exceeding 450°C, the oxidation rate gradually increases with a progressive weight gain from 1.00wt% to almost 3.00wt% with increasing temperature from 450 to 530°C. The compound exhibits an accelerated oxidation rate and increased weight gain of up to 12.00wt% at around 575°C. Upon reaching temperatures nearing 650°C, FeV_2O_4 undergoes almost complete oxidation with a relatively stable weight gain. For the $FeCr_2O_4$ sample, in Fig. 2(b), it gradually oxidizes at 280°C, with a sharp increase in the oxidation rate beyond 420°C. The weight gain caused by oxidation dramatically increases from approximately 0.50wt% at 400°C to about an average value of 2.50wt% within the range of 480–520°C. Further increasing to 900°C slows down the oxidation rate, while the weight gain progressively increases to approximately 3.50wt%. These results show that FeV_2O_4 and $FeCr_2O_4$ at different heating rates exhibit similar final weight gains, which are close to theoretical values of approximately 18.00wt% and 3.57wt%, respectively.

Fig. 3 presents the differential thermogravimetry (DTG) curves of FeV_2O_4 and $FeCr_2O_4$. The peak temperature of the DTG curves almost shifts toward a high temperature from 5 to 15 K/min, which can be attributed to heat transfer issues

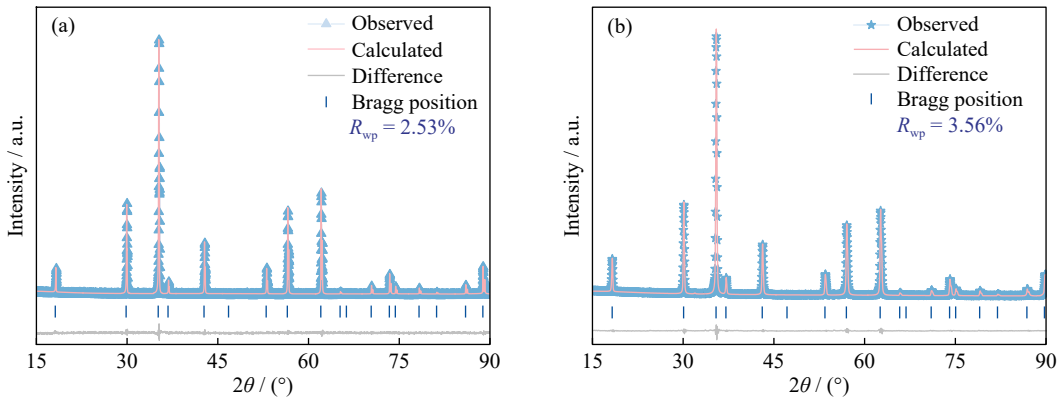

Fig. 1. XRD and Rietveld graphs of the synthesized (a) FeV_2O_4 and (b) $FeCr_2O_4$.

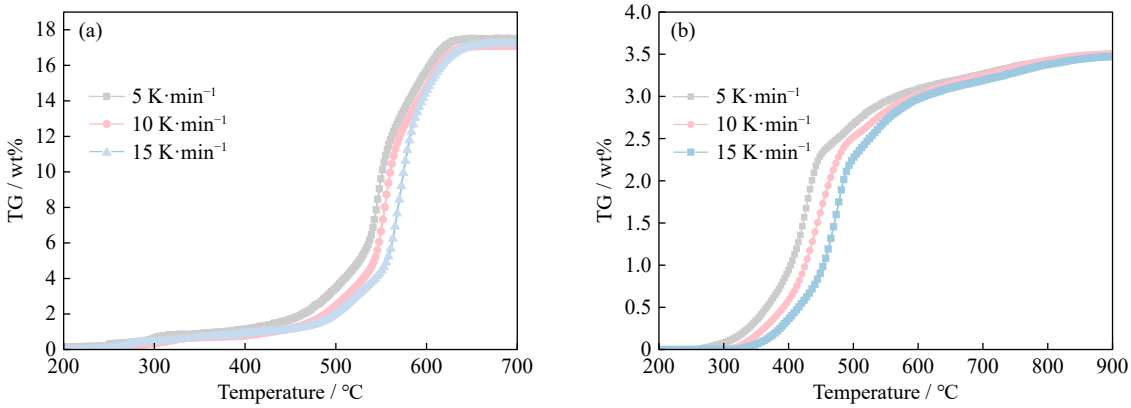

Fig. 2. TG curves of (a) FeV_2O_4 and (b) $FeCr_2O_4$ at different heating rates.

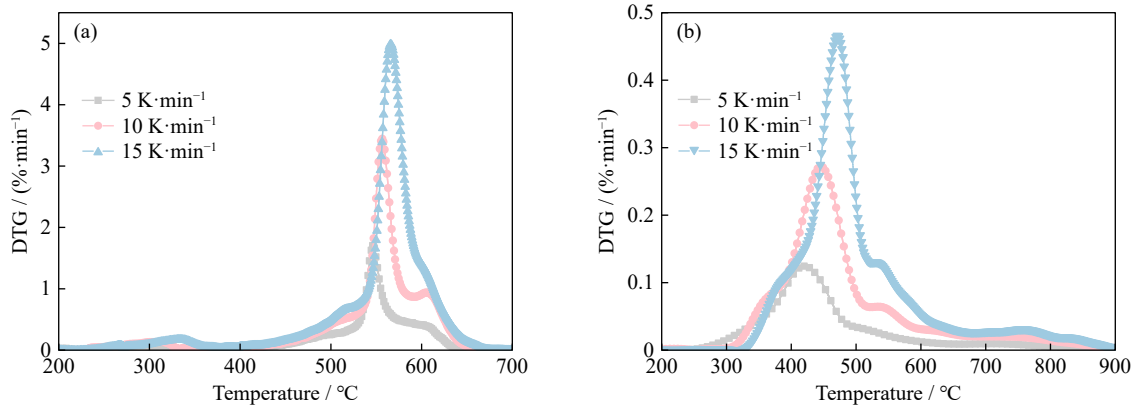

Fig. 3. DTG curves of (a) FeV_2O_4 and (b) $FeCr_2O_4$ at different heating rates.

between the sample and instrument. In Fig. 3, both samples display four distinct peaks, representing the four stages of their oxidation. For the FeV_2O_4 sample, in the initial stage, a stable minor peak is observed below 463°C. In the second stage, a small platform appears at 463–543°C, with a sample weight gain of 2.72wt%–3.78wt%. In the third stage, an evident DTG peak is observed at 531–594°C, with a sample weight gain of 8.07wt%–9.94wt%. In the final stage, a peak is observed at 575–668°C, with a sample weight gain of 3.30wt%–3.98wt%. Similarly, for $FeCr_2O_4$, the initial stage is represented by a small inflection point at 344–423°C, with a sample weight gain of 0.38wt%–0.53wt%. The second stage emerges at 363–525°C, with a sample weight gain of 1.92wt%–2.23wt%. In the third stage, a peak is observed at 495–633°C, with a sample weight gain of 0.45wt%–0.78wt%. In the final stage, a peak occurs at 600–876°C, with a sample weight gain of 0.37wt%–0.45wt%.

3.3. Oxidation degree analysis

Thermal kinetics analysis can measure the process of a chemical reaction (or phase transition). Among these, non-isothermal thermal analysis is the most widely used at multiple heating rates. In nonisothermal kinetic experiments, sample mass is related to temperature change, and the rule for changes in conversion rate under a specific heating rate is [30]:

$$\frac{d\alpha}{dt} = k(T)f(\alpha) \tag{1}$$

For dynamic data obtained at a specific heating rate $\beta = dT/dt$, $k(T)$ refers to the reaction rate constant and follows the Arrhenius equation $k(T) = A\exp[-E_a/(RT)]$. Then, Eq. (1) becomes:

$$\beta\frac{d\alpha}{dT} = A\exp\left(\frac{-E_a}{RT}\right)f(\alpha) \tag{2}$$

where E_a represents the apparent activation energy (kJ/mol), A represents the Arrhenius pre-exponential factor (s^{-1}), β represents the heating rate (K/min), R represents the universal gas constant (8.314 $J\cdot mol^{-1}\cdot K^{-1}$), T represents the absolute temperature (K), t represents the time (s), and α is the degree of conversion and measures the extent of completion of a reaction as follows:

$$\alpha = \frac{m_0 - m_t}{m_0 - m_f} \tag{3}$$

where m_0 refers to the initial mass of the sample (mg), m_t refers to the mass of the sample at time t (mg), and m_f refers to the final mass of the sample after the reaction (mg).

Fig. 4 presents the α versus T curves at different heating rates for the oxidation reactions of FeV_2O_4 and $FeCr_2O_4$. The conversion degrees of FeV_2O_4 and $FeCr_2O_4$ exhibit similar trends at different heating rates, i.e., an initial gradual increase, then a rapid ascent, and finally a stable plateau. Increasing the heating rate from 5 to 15 K/min results in a shift in the conversion rate toward higher temperatures. The conversion rate of FeV_2O_4 is relatively slow below 450°C, while that of $FeCr_2O_4$ is slower below 350°C. In 500–600°C for FeV_2O_4 and 400–600°C for $FeCr_2O_4$, the oxidation rates are significantly accelerated with show sharp increases in conversion degree. The complete oxidation of FeV_2O_4 occurs approximately at 600–700°C, as shown in Fig. 4(a). However, a gradual growth trend is still observed for $FeCr_2O_4$ at 650–900°C, as shown in Fig. 4(b), with complete oxidation occurring near 900°C.

Fig. 5 shows the first derivatives of the conversion degree of FeV_2O_4 and $FeCr_2O_4$ versus time. The oxidation rates of both compounds exhibit significant variations throughout the entire reaction process. The curve of FeV_2O_4 shows four stages of oxidation: stage I ($0.10 < \alpha < 0.22$–0.26), stage II (0.22–$0.26 < \alpha < 0.45$–0.48), stage III (0.45–$0.48 < \alpha < 0.70$–0.80), and stage IV (0.70–$0.80 < \alpha < 1.00$). Similarly, the oxidation process of $FeCr_2O_4$ also shows four stages: stage I ($0.10 < \alpha < 0.13$–0.17), stage II (0.13–$0.17 < \alpha < 0.43$–0.45), stage III (0.43–$0.45 < \alpha < 0.68$–0.73), and stage IV (0.68–$0.73 < \alpha < 1.00$).

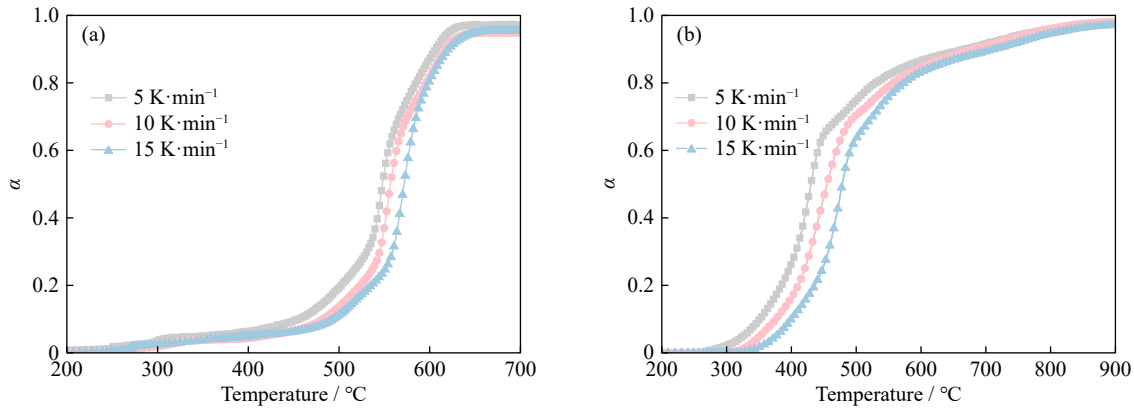

Fig. 4. α versus T curves for the oxidation of (a) FeV_2O_4 and (b) $FeCr_2O_4$.

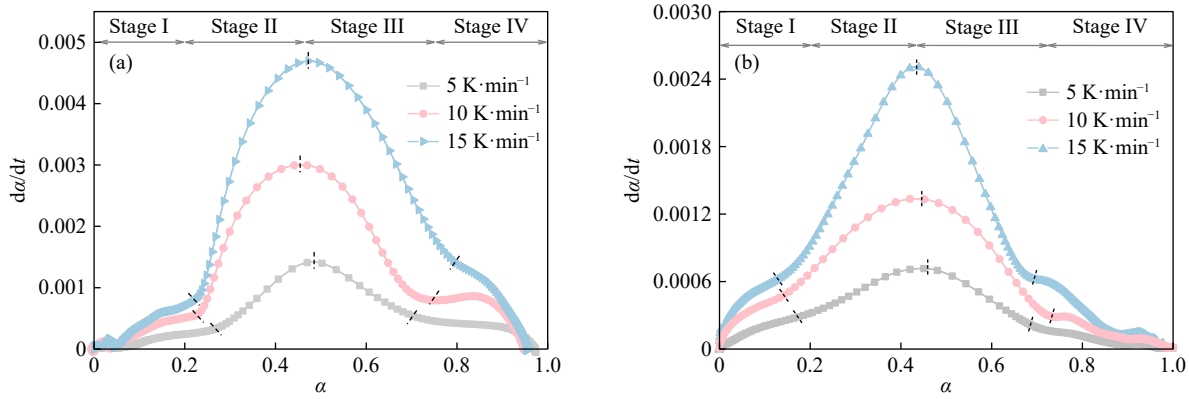

Fig. 5. First derivatives of conversion degree (α) versus time (t) at different heating rates for (a) FeV_2O_4 and (b) $FeCr_2O_4$.

3.4. Reaction activation energy

The isoconversional method is widely used because it determines a relatively reliable activation energy value, neglecting the chemical reaction mode function. Herein, the Kissinger–Akahira–Sunose (KAS) method was used to determine the activation energies of FeV_2O_4 and $FeCr_2O_4$ by nonisothermal thermal analysis.

The KAS formula can be expressed as [31–32],

$$\ln\left(\frac{\beta}{T_\alpha^2}\right) = \ln\left(\frac{AR}{E_\alpha G(\alpha)}\right) - \frac{E_\alpha}{RT_\alpha} \quad (4)$$

where T_α represents the thermodynamic temperature corresponding to the specified α value, E_α represents the activation energy (kJ/mol) corresponding to the specified α value, and $G(\alpha)$ represents the integral form of the kinetic mode function. The T_α corresponding to the same α value is taken at different heating rates. Apparent activation energy can be obtained from the ln (β/T^2) versus $1/T$ plot for a given value of conversion degree (α), where the slope is equal to $-E_\alpha/R$. Fig. 6 presents the ln (β/T^2) against $1/T$ plots of FeV_2O_4 and $FeCr_2O_4$ for α of 0.10–0.90 with a step of 0.05.

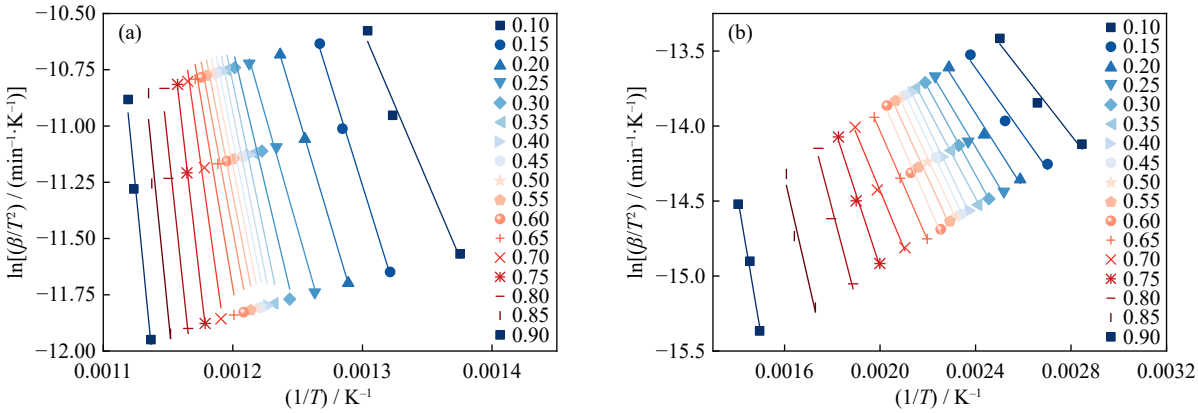

Fig. 6. Determination of activation energy by the KAS method: (a) FeV_2O_4; (b) $FeCr_2O_4$.

Fig. 7 shows the variation in the activation energy of the oxidation of FeV_2O_4 and $FeCr_2O_4$ with conversion degree by the KAS method. The apparent activation energy for the oxidation of FeV_2O_4 is much higher and more varied than that of $FeCr_2O_4$, indicating greater complexity in the oxidation mechanism of FeV_2O_4 than $FeCr_2O_4$. This suggests that a higher activation energy is required for the transition of reactant molecules from the ground state to the activated state in FeV_2O_4. This also indicates that the reaction pathway of $FeCr_2O_4$ may be simpler and more direct than FeV_2O_4, without significant energy barriers or obstacles. In addition, the higher apparent activation energy of FeV_2O_4 implies the great influence of temperature on the oxidation of FeV_2O_4, while $FeCr_2O_4$ displays higher thermal stability, as depicted by its higher maximum oxidation temperature than that of FeV_2O_4.

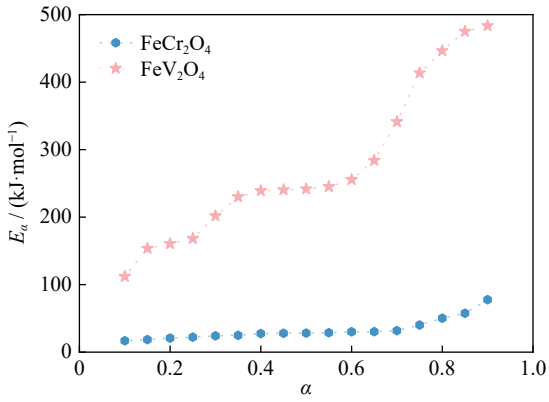

Fig. 7. Activation energy versus conversion degree plots of FeV_2O_4 and $FeCr_2O_4$ oxidation.

The apparent activation energy of FeV_2O_4 oxidation displays significant variations, which can be roughly divided into four stages based on the previous analysis. In the first stage, the activation energy gradually increases from 112.00 to 160.50 kJ/mol with the progression of the oxidation reaction. In the second stage, a slight elevation in activation energy is observed between 160.50 and 240.80 kJ/mol during ongoing oxidation reactions. In the third stage, a rapid escalation in activation energy occurs, elevating it from 240.80 to 413.40 kJ/mol alongside the oxidation reaction process. In the fourth stage, an ultimate increase in activation energy up to 483.40 kJ/mol is observed due to continued oxidation. For $FeCr_2O_4$, its apparent activation energy shows a slight increase from 16.90 to 32.00 kJ/mol below a conversion degree of about 0.70. Further increasing the conversion degree from about 0.70 to 0.90 results in a significant increase in apparent activation energy to 77.60 kJ/mol, demonstrating the increase in difficulty in the later stages of the oxidation process compared with the earlier stages. It can also be observed that during the linear heating process, the conversion degree of $FeCr_2O_4$ can quickly increase from 0 to about 0.7 at 300–500°C, while it only gradually increases from about 0.70 to approximately 1.00 at 500–900°C, as shown in Fig. 4(b). The nonlinear changes of different conversion degrees and apparent activation energies of FeV_2O_4 and $FeCr_2O_4$ imply an inconsistent reaction mechanism throughout the oxidation process, indicating the presence of multiple competitive reactions, as further supported by the DTG results.

3.5. Reaction model analysis

The Malek method is a kinetic analysis method based on the multiheating rate method that can be used to determine the reaction mechanism and is widely accepted for its simplicity and accuracy [33–34].

According to the reaction rate Eq. (5) and the Coats–Redfern Eq. (6) [35],

$$\frac{d\alpha}{dt} = A\exp\left(-\frac{E}{RT}\right)f(\alpha) \quad (5)$$

$$G(\alpha)=\int_0^{\alpha}\frac{\mathrm{d}\alpha}{f(\alpha)}=\frac{ART_{\alpha}^2}{E\beta}\exp\left(-\frac{E}{RT_{\alpha}}\right) \tag{6}$$

It can be concluded that:

$$G(\alpha)=\frac{RT_{\alpha}^2}{E\beta}\frac{\mathrm{d}\alpha}{\mathrm{d}t}\frac{1}{f(\alpha)} \tag{7}$$

When $\alpha = 0.5$,

$$G(0.5)=\frac{RT_{0.5}^2}{E\beta}\left(\frac{\mathrm{d}\alpha}{\mathrm{d}t}\right)_{0.5}\frac{1}{f(0.5)} \tag{8}$$

where $(\mathrm{d}\alpha/\mathrm{d}t)_{0.5}$ represents the reaction rate during the whole reaction process when $\alpha = 0.5$. $Y(\alpha)$ and $y(\alpha)$ are defined by the ratio of Eqs. (7)–(8). Consequently, Eqs. (9)–(10) can be obtained as

$$Y(\alpha)=\left(\frac{T}{T_{0.5}}\right)^2\frac{\left(\frac{\mathrm{d}\alpha}{\mathrm{d}t}\right)}{\left(\frac{\mathrm{d}\alpha}{\mathrm{d}t}\right)_{0.5}}=\frac{f(\alpha)\cdot G(\alpha)}{f(0.5)\cdot G(0.5)} \tag{9}$$

and

$$y(\alpha)=\left(\frac{T_i}{T_{0.5}}\right)^2\frac{\left(\frac{\mathrm{d}\alpha}{\mathrm{d}t}\right)_i}{\left(\frac{\mathrm{d}\alpha}{\mathrm{d}t}\right)_{0.5}} \tag{10}$$

where T_i and $(\mathrm{d}\alpha/\mathrm{d}t)_i$ represent the temperature and reaction rate at the point α_i, respectively.

In this study, the most probable $f(\alpha)$ is determined based on the standard curve $y(\alpha)$–α. The relationship between actual $y(\alpha)$ and α can be obtained by experimental data with three heating rates. If the experimental data curve coincides with or if all the experimental data points fall on a standard curve, then $f(\alpha)$ or $G(\alpha)$ corresponding to that standard curve is determined as the most likely kinetic mechanism function. Fig. 8 illustrates the relationship between the standard curve $y(\alpha)$ and the experimental curve $y(\alpha)$ of FeV_2O_4 and $FeCr_2O_4$ oxidation.

For FeV_2O_4, in the conversion degree of 0.10–0.26, the three experimental curves agree well with the No. 35 standard curve. The function corresponding to curve 35 is the reaction series equation, the mechanism is $n = 4$, and the differential form of the mechanism function $f(\alpha)=\frac{1}{4}(1-\alpha)^{-3}$ is the integral $G(\alpha)=1-(1-\alpha)^4$. No satisfactory correlation with any curve is observed in the second and third stage ranges, suggesting the presence of multiple oxidation mechanisms for FeV_2O_4 at this stage, resulting in poor agreement with experimental data, requiring further analysis to elucidate the specific mechanism function. During the progression of the reaction, as the experimental curve ranges from 0.68 to 0.95, the $\beta = 5$ K/min curve gradually approaches the standard curves of 39 and 40 (following an exponential law). The curves obtained at $\beta = 10$ and 15 K/min closely resemble the standard curves of 36, 38, and 41, which correspond to chemical reactions.

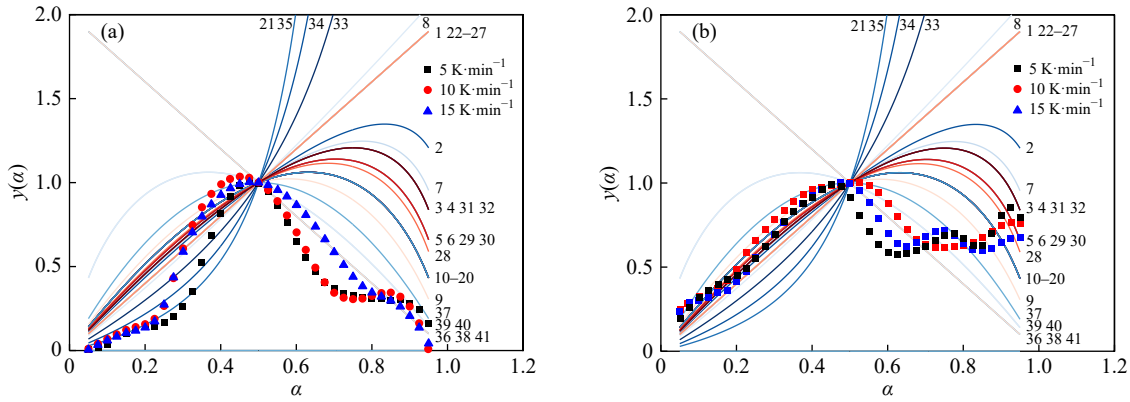

Fig. 8. Experimental data points and standard curves of (a) FeV_2O_4 and (b) $FeCr_2O_4$ by the Malek method.

For $FeCr_2O_4$, the three experimental curves display characteristics of the three-position diffusion model in the first and second stages, but the involved specific mechanism function requires further analysis. Notably, the experimental curve in conversion degree 0.43–0.95 is similar to that of FeV_2O_4, demonstrating multiple mechanism functions. Combined with the KAS results, this stage represents the gradual transition process from a three-dimensional diffusion model to a chemical reaction.

3.6. *In-situ* XRD analysis

In-situ XRD was performed to describe the oxidation process of FeV_2O_4 and $FeCr_2O_4$, as shown in Fig. 9. The diffraction peak intensity of FeV_2O_4 gradually decreases, while those of Fe_3O_4, V_2O_3, and Fe_2O_3 gradually increase at 200–450°C, as shown in Fig. 9(a). At 500–650°C, most of the intermediates are oxidized, which results in the identification of the diffraction peaks corresponding to VO_2, V_6O_{13}, and FeV_2O_4. The oxidation state of vanadium gradually shifts from V^{3+} and V^{4+} to V^{5+}, forming vanadium pentoxide, which has a relatively low melting point of 943 K (670°C). Because vanadium pentoxide volatilization or continuous production of vanadium pentoxide may exist in liquid and amorphous states [36–37], where there is not much volatilization and more of it is in the melting state, the intensity of the diffraction peak is significantly reduced. However, in the oxidation process, the oxidized Fe/V ratio changes and the volatilization of vanadium pentoxide is about 0.2% [38–39], resulting

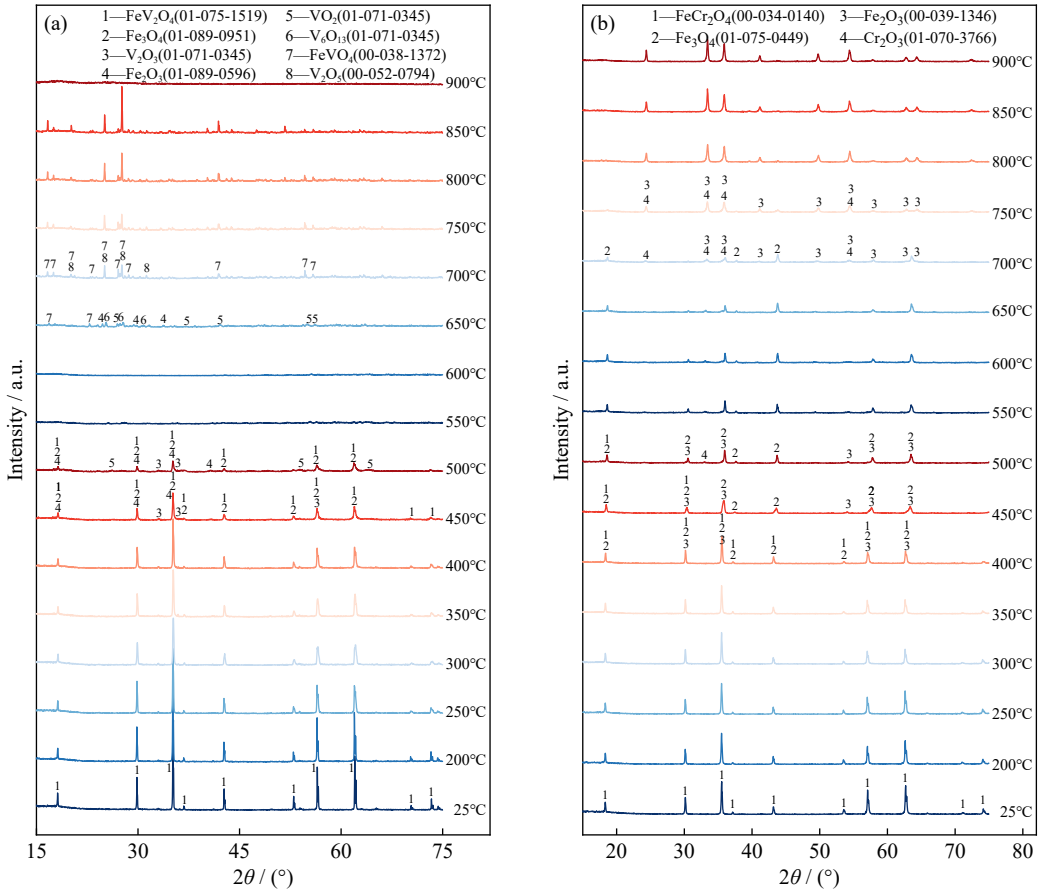

Fig. 9. ***In-situ*** **XRD patterns of (a) FeV_2O_4 and (b) $FeCr_2O_4$ at different temperatures.**

in a reduction in vanadium in the sample but relatively small compared with the total sample. Above 700°C, the diffraction peaks corresponding to FeV_2O_4 vanish, while those of $FeVO_4$ and V_2O_5 as final products tend to stabilize.

In Fig. 9(b), the oxidation process of $FeCr_2O_4$ is similar to that of FeV_2O_4. At 200–400°C, the diffraction peak intensity of $FeCr_2O_4$ gradually decreases. At 450–700°C, the diffraction peak changes and new substances are produced. Finally, above 750°C, the diffraction peak intensities of Fe_2O_3 and Cr_2O_3 gradually increase and become stable, demonstrating complete oxidation reaction.

3.7. Derivation of the oxidation mechanism

3.7.1. Derivation of the FeV_2O_4 oxidation mechanism

The oxidation process of FeV_2O_4 is highly intricate, involving numerous intermediates. Based on the *in-situ* XRD and TG-DTG results, the oxidation pathway of FeV_2O_4 is outlined as follows. In the initial oxidation stage of FeV_2O_4 (200–450°C), the reaction is

$$6FeV_2O_4 + O_2 = 2Fe_3O_4 + 6V_2O_3 \quad (11)$$

As the temperature continues to increase, the oxidation reactions that may occur in the middle oxidation stage (450–700°C) are

$$4Fe_3O_4 + O_2 = 6Fe_2O_3 \quad (12)$$

$$2V_2O_3 + O_2 = 4VO_2 \quad (13)$$

$$1.5V_2O_3 + O_2 = 0.5V_6O_{13} \quad (14)$$

$$4VO_2 + O_2 = 2V_2O_5 \quad (15)$$

$$12VO_2 + O_2 = 2V_6O_{13} \quad (16)$$

$$V_6O_{13} + O_2 = 3V_2O_5 \quad (17)$$

$$4Fe_3O_4 + 6V_2O_5 + O_2 = 12FeVO_4 \quad (18)$$

$$Fe_2O_3 + V_2O_5 = 2FeVO_4 \quad (19)$$

Previous work [40] has confirmed the presence of solid solution FeV_2O_6 formed by oxidation of FeV_2O_4 at 470–580°C, which is formed through oxidation of FeV_2O_4. However, no FeV_2O_6 phase was detected in this study from the *in-situ* XRD results, suggesting the possibility of a subsequent rapid oxidation reaction occurring for FeV_2O_6 as an intermediate.

$$FeV_2O_4 + O_2 = FeV_2O_6 \quad (20)$$

$$8FeV_2O_6 + O_2 = V_6O_{13} + 8FeVO_4 + V_2O_5 \quad (21)$$

$$12FeV_2O_6 + O_2 = 2V_6O_{13} + 12FeVO_4 \quad (22)$$

Adding the three formulas, the total reaction equation is

$$0.8FeV_2O_4 + O_2 = 0.8FeVO_4 + 0.4V_2O_5 \quad (23)$$

The oxidation mechanism of FeV_2O_4 was further confirmed by calculations of the Gibbs-free energies of the chemical reactions at each stage. In Fig. 10, all reactions exhibit $-\Delta G$ values across the entire temperature range considered, indicating their possibility. Reactions (18) and (12) involving Fe_3O_4 have the lowest ΔG values at temperatures

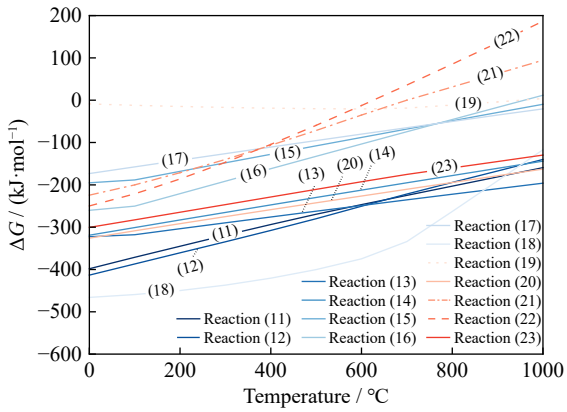

Fig. 10. Gibbs-free energy changes for possible reactions during the FeV_2O_4 oxidation.

below 850 and 600°C, respectively, suggesting their greater propensity toward oxidation reactions. The intermediate V_2O_3 undergoes easy oxidation to generate VO_2, which is further oxidized to V_6O_{13} and V_2O_5. Reactions (21) and (22) can only spontaneously react below 640 and 590°C, respectively. As the reaction progresses, Fe_2O_3 and V_2O_5 eventually react to form $FeVO_4$ (reaction (19)).

From the above analysis, the oxidation pathway of FeV_2O_4 oxidation in air can be derived and is illustrated in Fig. 11.

3.7.2. Derivation of the $FeCr_2O_4$ oxidation mechanism

The oxidation process of $FeCr_2O_4$ is relatively straightforward. Based on the *in-situ* XRD and TG-DTG results, $FeCr_2O_4$ does not oxidize during the initial stage (200–400°C). However, significant changes in the XRD pattern are observed during the middle oxidation stage (450–700°C), indicating the potential occurrence of oxidation reactions.

$$6FeCr_2O_4 + O_2 = 2Fe_3O_4 + 6Cr_2O_3 \quad (24)$$

$$0.6FeCr_2O_4 + O_2 = 0.2Fe_3O_4 + 1.2CrO_3 \quad (25)$$

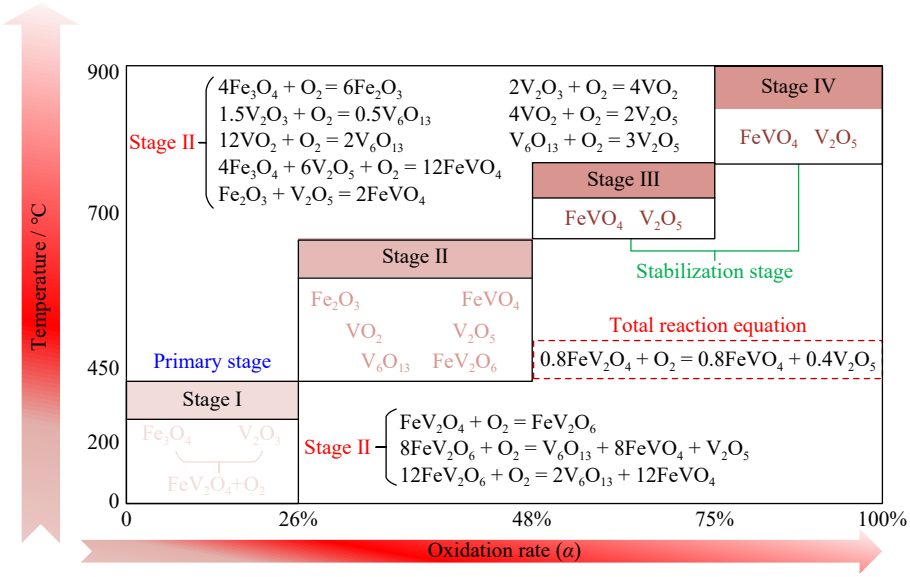

Fig. 11. Schematic of the oxidation pathway of FeV_2O_4.

The Gibbs-free energy of reaction (25) is observed to be greater than 0 in 0–1000°C, as depicted in Fig. 12, suggesting that under the experimental conditions, chromium did not undergo oxidation to the hexavalent state.

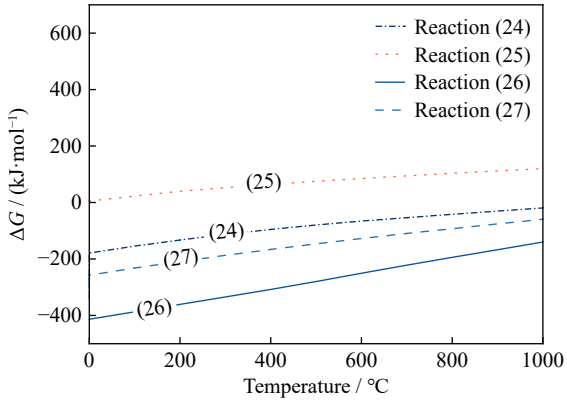

Fig. 12. Gibbs-free energy changes for possible reactions during the $FeCr_2O_4$ oxidation process.

With increasing temperature, Fe_3O_4 can also react with air to form Fe_2O_3.

$$4Fe_3O_4 + O_2 = 6Fe_2O_3 \quad (26)$$

The oxidation of $FeCr_2O_4$ basically stops above 700°C, yielding Fe_2O_3 and Cr_2O_3 as the final products. Thus, the total reaction is

$$4FeCr_2O_4 + O_2 = 2Fe_2O_3 + 4Cr_2O_3 \quad (27)$$

The Gibbs-free energies of reactions (24), (26), and (27) in air from 0 to 1000°C are shown in Fig. 12. These reactions exhibit $-\Delta G_r$ values within this temperature range, indicating their possibility. Notably, the ΔG_r value of reaction (25) is more negative than that of reaction (24), suggesting the oxidation of Fe_3O_4 from reaction (24) to Fe_2O_3.

Based on the above analysis, the oxidation pathway of $FeCr_2O_4$ in air can be derived and is illustrated in Fig 13.

Based on the above comprehensive analysis, both the oxidation mechanisms of spinel FeV_2O_4 and spinel $FeCr_2O_4$ are

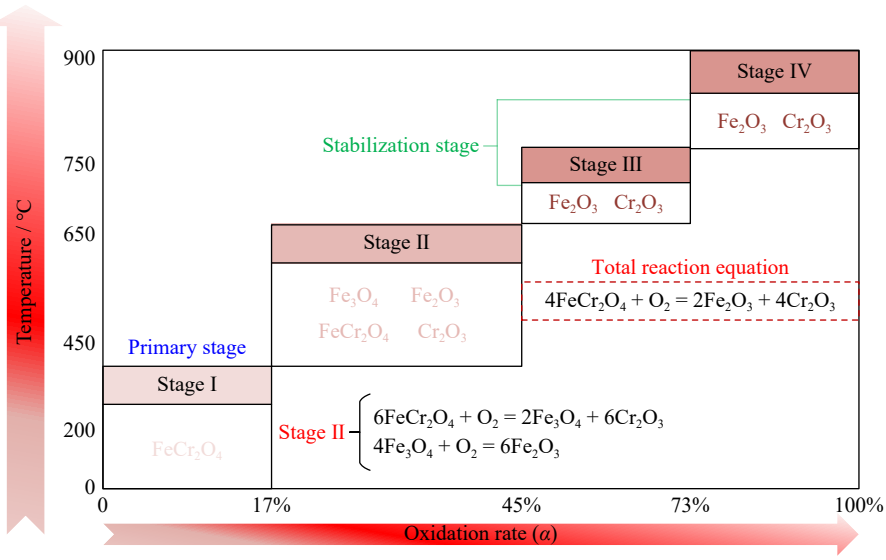

Fig. 13. Schematic of the oxidation pathway of $FeCr_2O_4$.

highly intricate. Furthermore, thoroughly exploring their oxidation behavior has significant implications for practical applications. For instance, during the roasting process of vanadium and chromium slag, spinel FeV_2O_4 and spinel $FeCr_2O_4$ serve as the main phases of the slag. By controlling the degree of oxidation for these spinel phases, optimization of the leaching and extraction processes for vanadium and chromium can be performed for improvement in recovery rates and reduction in production costs. In fact, researchers have utilized the differences in oxidation, conversion, and thermodynamics between ferrovanadium spinel and ferrochrome spinel in the roasting process to extract vanadium and chromium by different techniques such as two-stage roasting, fractional roasting, and selective extraction of vanadium [27,41–43]. These methods also emphasize the importance of fully understanding the oxidation mechanism of ferrovanadium and ferrochrome spinels. This work provides technical support for efficient, green, and low-carbon recovery of vanadium and chromium from vanadium chromium slag, thus improving resource utilization capabilities.

4. Conclusions

The following conclusions can be drawn:

(1) The oxidation process of FeV_2O_4 and $FeCr_2O_4$ can be divided into four stages. The third stage has the significant contribution to the weight gain of FeV_2O_4, with an increase of 8.07wt%–9.94wt%. The second stage predominantly contributes to the weight gain of $FeCr_2O_4$, ranging from 1.92wt% to 2.23wt%.

(2) The oxidation of FeV_2O_4 has a much higher apparent activation energy than that of $FeCr_2O_4$. Their oxidation mechanisms are complex and have distinct mechanism functions. In particular, the chemical reaction controls the entire oxidation process for FeV_2O_4, whereas that for $FeCr_2O_4$ transitions from a three-dimensional diffusion model to a chemical reaction model.

(3) *In-situ* XRD results reveal numerous intermediate products during the oxidation process of both compounds, finally forming the final products $FeVO_4$ and V_2O_5 for FeV_2O_4 and Fe_2O_3 and Cr_2O_3 for $FeCr_2O_4$, respectively.

Acknowledgements

This work was supported by the National Natural Science Foundation of China (No. 52004044), the Natural Science Foundation of Chongqing, China (Nos. cstb2022nscq-msx0801 and cstc2021jcyj-msxmx0882), the Foundation of Chongqing University of Science and Technology (No. ckrc2022030), the Graduate Research Innovation Project of Chongqing University of Science and Technology (No. YKJCX2220216), and the National Undergraduate Training Program for Innovation and Entrepreneurship (No. 202311551007).

Conflict of Interest

The authors declare that they have no known competing financial interests or personal relationships that could have appeared to influence the work reported in this paper.

References

[1] V. Tsurkan, H.A.K. von Nidda, J. Deisenhofer, P. Lunkenheimer, and A. Loidl, On the complexity of spinels: Magnetic, electronic, and polar ground states, *Phys. Rep.*, 926(2021), p. 1.

[2] A. Sundaresan and N. Ter-Oganessian, Magnetoelectric and multiferroic properties of spinels, *J. Appl. Phys.*, 129(2021), art. No. 060901.

[3] L.G. Ren, Y.Q. Wang, X. Zhang, Q.C. He, and G.L. Wu, Efficient microwave absorption achieved through *in situ* construction of core–shell $CoFe_2O_4$@mesoporous carbon hollow spheres, *Int. J. Miner. Metall. Mater.*, 30(2023), No. 3, p. 504.

[4] N. Nishiguchi and M. Onoda, A pseudotetramer in the geometrically frustrated spinel system CdV_2O_4, *J. Phys.: Condens. Matter*, 14(2002), No. 28, p. L551.

[5] R. Batulin, M. Cherosov, A. Kiiamov, *et al.*, Synthesis and single crystal growth by floating zone technique of $FeCr_2O_4$

multiferroic spinel: Its structure, composition, and magnetic properties, *Magnetochemistry*, 8(2022), No. 8, p. 86.
[6] G.S. Pei, C. Pan, D.P. Zhong, J.Y. Xiang, and X.W. Lv, Crystal structure, phase transitions, and thermodynamic properties of magnesium metavanadate (MgV_2O_6), *J. Magnesium Alloys*, 12(2024), No. 4, p. 1449.
[7] S. Nishihara, W. Doi, H. Ishibashi, Y. Hosokoshi, X.M. Ren, and S. Mori, Appearance of magnetization jumps in magnetic hysteresis curves in spinel oxide FeV_2O_4, *J. Appl. Phys.*, 107(2010), No. 9, art. No. 09A504.
[8] L. Yang, Y.R. Zhang, C.P. Wu, *et al*., A novel high-selectivity mixed potential ammonia gas sensor based on $FeCr_2O_4$ sensing electrode, *J. Electroanal. Chem.*, 924(2022), art. No. 116849.
[9] H.F. Shang and D.G. Xia, Spinel $LiMn_2O_4$ integrated with coating and doping by Sn self-segregation, *Int. J. Miner. Metall. Mater.*, 29(2022), No. 5, p. 909.
[10] B. Shi, H.S. Liang, Z.J. Xie, Q. Chang, and H.J. Wu, Dielectric loss enhancement induced by the microstructure of $CoFe_2O_4$ foam to realize broadband electromagnetic wave absorption, *Int. J. Miner. Metall. Mater.*, 30(2023), No. 7, p. 1388.
[11] G. Ghanashyam and H.K. Jeong, Synthesis of nitrogen-doped plasma treated carbon nanofiber as an efficient electrode for symmetric supercapacitor, *J. Energy Storage*, 33(2021), art. No. 102150.
[12] H. Zhang, G.F. Qian, T.Q. Yu, J.L. Chen, L. Luo, and S.B. Yin, Interface Engineering of Ni_3Fe and FeV_2O_4 coupling with carbon-coated mesoporous nanosheets for boosting overall water splitting at 1500 $mA{\cdot}cm^{-2}$, *ACS Sustainable Chem. Eng.*, 9(2021), No. 24, p. 8249.
[13] I.V.B. Maggay, L.M.Z. De Juan, J.S. Lu, *et al*., Electrochemical properties of novel FeV_2O_4 as an anode for Na-ion batteries, *Sci. Rep.*, 8(2018), art. No. 8839.
[14] T.R. Kuo, W.T. Chen, H.J. Liao, *et al*., Improving hydrogen evolution activity of earth-abundant cobalt-doped iron pyrite catalysts by surface modification with phosphide, *Small*, 13(2017), No. 8, art. No. 1603356.
[15] S. Yougbare, T.K. Chang, S.H. Tan, *et al*., Antimicrobial gold nanoclusters: Recent developments and future perspectives, *Int. J. Mol. Sci.*, 20(2019), No. 12, art. No. E2924.
[16] S. Yougbaré, H.L. Chou, C.H. Yang, *et al*., Facet-dependent gold nanocrystals for effective photothermal killing of bacteria, *J. Hazard. Mater.*, 407(2021), art. No. 124617.
[17] B. Janani, S. Swetha, A. Syed, *et al*., Spinel FeV_2O_4 coupling on nanocube-like Bi_2O_3 for high performance white light photocatalysis and antibacterial applications, *J. Alloys Compd.*, 887(2021), art. No. 161432.
[18] A. Chinnathambi, Synthesis and characterization of spinel FeV_2O_4 coupled ZnO nanoplates for boosted white light photocatalysis and antibacterial applications, *J. Alloys Compd.*, 890(2022), art. No. 161742.
[19] A. Abbasi, A.H. Keihan, M.A. Golsefidi, M. Rahimi-Nasrabadi, and H. Khojasteh, Synthesis, characterization and photocatalytic activity of $FeCr_2O_4$ and $FeCr_2O_4$/Ag nanocomposites, *J. Nanostruct.*, 10(2020), No. 3, p. 518.
[20] A.V. Borhade, D.R. Tope, J.A. Agashe, and S.S. Kushare, Synthesis, characterization and photocatalytic study of $FeCr_2O_4$@ZnO@MgO core–shell nanoparticle, *J. Water Environ. Nanotechnol.*, 6(2021), No. 2, p. 164.
[21] C.P.J. Van Vuuren and P.P. Stander, The oxidation of FeV_2O_4 by oxygen in a sodium carbonate mixture, *Miner. Eng.*, 14(2001), No. 7, p. 803.
[22] A. Wold, D.B. Rogers, R. Arnott, and N. Menyuk, Vanadium iron oxides, *J. Appl. Phys.*, 33(1962), p. 1208.
[23] F. Paborji, M.S. Afarani, A.M. Arabi, and M. Ghahari, Solution combustion synthesis of $FeCr_2O_4$ powders for pigment applications: Effect of fuel type, *Int. J. Appl. Ceram. Technol.*, 19(2022), No. 5, p. 2406.
[24] Y. Hidaka, T. Anraku, and N. Otsuka, Deformation and fracture behavior of surface oxide scale on Fe–13Cr alloy in hot-rolling process, *Mater. Sci. Forum*, 522-523(2006), p. 461.
[25] X. Zhang, B. Xie, J. Diao, and X.J. Li, Nucleation and growth kinetics of spinel crystals in vanadium slag, *Ironmaking Steelmaking*, 39(2012), No. 2, p. 147.
[26] H.G. Wang, M.Y. Wang, and X.W. Wang, Leaching behaviour of chromium during vanadium extraction from vanadium slag, *Miner. Process. Extr. Metall.*, 124(2015), No. 3, p. 127.
[27] H.Y. Li, H.X. Fang, K. Wang, *et al*., Asynchronous extraction of vanadium and chromium from vanadium slag by stepwise sodium roasting–water leaching, *Hydrometallurgy*, 156(2015), p. 124.
[28] S. Nakamura and A. Fuwa, Distinct evidence of orbital order in spinel oxide FeV_2O_4 by ^{57}Fe mössbauer spectroscopy, *J. Phys. Soc. Jpn.*, 85(2016), No. 1, art. No. 014702.
[29] S. Nakamura, K. Tasaki, and T. Katsufuji, Competitive local structure in mixed vanadium spinel $Fe_{1-x}Mn_xV_2O_4$, [in] *Proceedings of the International Conference on Strongly Correlated Electron Systems* (*SCES2019*), Okayama, 2019.
[30] G. Cohn, Reactions in the solid state, *Chem. Rev.*, 42(1948), No. 3, p. 527.
[31] H.E. Kissinger, Variation of peak temperature with heating rate in differential thermal analysis, *J. Res. Natl. Bur. Stand.*, 57(1956), No. 4, art. No. 217.
[32] T. Ozawa, Estimation of activation energy by isoconversion methods, *Thermochim. Acta*, 203(1992), p. 159.
[33] M.A. Arshad, A. Maaroufi, R. Benavente, J.M. Pereña, and G. Pinto, Thermal degradation kinetics of insulating/conducting epoxy/Zn composites under nonisothermal conditions, *Polym. Compos.*, 34(2013), No. 12, p. 2049.
[34] J. Málek, The kinetic analysis of non-isothermal data, *Thermochim. Acta*, 200(1992), p. 257.
[35] A.W. Coats and J.P. Redfern, Kinetic parameters from thermogravimetric data, *Nature*, 201(1964), p. 68.
[36] T. Shyrokykh, X.W. Wei, S. Seetharaman, and O. Volkova, Vaporization of vanadium pentoxide from $CaO–SiO_2–VO_x$ slags during alumina dissolution, *Metall. Mater. Trans. B*, 52(2021), No. 3, p. 1472.
[37] Y. Yang, L.D. Teng, and S. Seetharaman, Kinetic studies on evaporation of liquid vanadium oxide, VO_x (where x = 4 or 5), *Metall. Mater. Trans. B*, 43(2012), No. 6, p. 1684.
[38] D.T. Cestarolli and E.M. Guerra, Vanadium pentoxide (V_2O_5): Their obtaining methods and wide applications, [in] *Transition Metal Compounds—Synthesis*, *Properties*, *and Application*, IntechOpen, Vienna, 2021.
[39] W.X. Wang, Z.L. Xue, S.Q. Song, *et al*., Research on high-temperature volatilization characteristics of V_2O_5 during direct alloying of smelting vanadium steel, *Adv. Mater. Res.*, 557-559(2012), p. 182.
[40] P.P. Stander and C.P.J. Van Vuuren, The high temperature oxidation of FeV_2O_4, *Thermochim. Acta*, 157(1990), No. 2, p. 347.
[41] J. Wen, T. Jiang, Y.Z. Xu, J.Y. Liu, and X.X. Xue, Efficient separation and extraction of vanadium and chromium in high chromium vanadium slag by selective two-stage roasting–leaching, *Metall. Mater. Trans. B*, 49(2018), No. 3, p. 1471.
[42] H.Y. Li, J. Cheng, C.J. Wang, S. Shen, J. Diao, and B. Xie, Eco-friendly selective extraction of vanadium from vanadium slag with high chromium content via magnesiation roasting–acid leaching, *Metall. Mater. Trans. B*, 53(2022), No. 1, p. 604.
[43] J.Y. Xiang, X. Wang, G.S. Pei, Q.Y. Huang, and X.W. Lü, Recovery of vanadium from vanadium slag by composite roasting with CaO/MgO and leaching, *Trans. Nonferrous Met. Soc. China*, 30(2020), No. 11, p. 3114.